# Latitudinal transport by barotropic waves in Titan's stratosphere. II. Results from a coupled dynamics–microphysics–photochemistry GCM

D. Luz,[a,b,*] F. Hourdin,[c] P. Rannou,[d] and S. Lebonnois[c]

[a] *Observatório Astronómico de Lisboa, Tapada da Ajuda, 1349-018 Lisboa, Portugal*
[b] *LESIA-Observatoire de Paris-Meudon (bat. du LAM) 5, Place Jules Janssen, F-92195 Meudon Cedex, France*
[c] *Laboratoire de Météorologie Dynamique, Jussieu, CNRS/UPMC, Box 99, F-75252 Paris Cedex 05, France*
[d] *Service d'Aéronomie, Jussieu, CNRS/UPMC, Box 102, F-75252 Paris Cedex 05, France*

## Abstract

We present a 2D general circulation model of Titan's atmosphere, coupling axisymmetric dynamics with haze microphysics, a simplified photochemistry and eddy mixing. We develop a parameterization of latitudinal eddy mixing by barotropic waves based on a shallow-water, longitude–latitude model. The parameterization acts locally and in real time both on passive tracers and momentum. The mixing coefficient varies exponentially with a measure of the barotropic instability of the mean zonal flow. The coupled GCM approximately reproduces the Voyager temperature measurements and the latitudinal contrasts in the distributions of HCN and $C_2H_2$, as well as the main features of the zonal wind retrieved from the 1989 stellar occultation. Wind velocities are consistent with the observed reversal time of the North–South albedo asymmetry of 5 terrestrial years. Model results support the hypothesis of a non-uniform distribution of infrared opacity as the cause of the Voyager temperature asymmetry. Transport by the mean meridional circulation, combined with polar vortex isolation may be at the origin of the latitudinal contrasts of trace species, with eddy mixing remaining restricted to low latitudes most of the Titan year. We interpret the contrasts as a signature of non-axisymmetric motions.

## 1. Introduction

Titan's atmospheric circulation is dominated by an axisymmetric regime, with superrotating zonal winds and horizontal distributions of temperature, albedo and chemical compounds showing important latitudinal contrasts but very little longitudinal variations (Flasar et al., 1981; Sromovsky et al., 1981; Coustenis and Bézard, 1995). Barotropic planetary waves, which are thought to be crucial in the angular momentum cycle of superrotating atmospheres (Gierasch, 1975; Rossow and Williams, 1979), are probably an important component of the circulation that departs from axial symmetry. Planetary waves associated with equatorward, upgradient transport of angular momentum were identified in 3D simulations with modified terrestrial general circula-

tion models (GCMs) (Hourdin et al., 1992; Del Genio et al., 1993; Del Genio and Zhou, 1996) and with a GCM developed specifically for Titan (Hourdin et al., 1995, hereafter H95). In the numerical experiments the waves are mainly generated by barotropic instability of the mean zonal wind and thus are tightly coupled to the axisymmetric circulation.

In a previous paper (Luz and Hourdin, this issue, hereafter paper 1), we have used a shallow-water model to investigate the transport properties of barotropic waves in Titan's atmosphere. In the presence of a barotropically unstable mean zonal wind similar to the one retrieved from the 1989 occultation of 28 Sgr by Titan (Hubbard et al., 1993), barotropic waves tend to transport angular momentum from the high-latitude jet into its equatorward flank, thereby reducing the instability. This transport, which is done against the gradient of angular momentum, tends to homogenize the potential vorticity (PV) (paper 1, see also Allison et al., 1994). Although the largest latitudinal excursions of air parcels occur

---

* Corresponding author.
 *E-mail address:* luz@despace.obspm.fr (D. Luz).

around the latitude of the jet at 50°, the most important mixing takes place at the barotropically unstable region. This non-uniform mixing affects not only potential vorticity but also organic haze and chemical species such as HCN and $C_2H_2$, which showed significant latitudinal contrasts at the time of the Voyager encounter.

In order to study the latitudinal variations of the atmospheric composition and haze and the possible feedback cycles on atmospheric dynamics, we have been developing since 1997 a coupled GCM. Given the prohibitive cost of 3D modeling in the particular context of Titan (deep atmosphere, very long time constants compared to the dynamical time step, need for various sensitivity studies) and since variability is concentrated on the vertical and meridional structure in an atmosphere which appears to be close to axial symmetry, a 2D approach (latitude–altitude) has been made as a first approximation. Using a 2D chemistry-transport model, Lebonnois et al. (2001) first explained the latitudinal contrasts in hydrocarbons and nitriles observed by Voyager in Titan's stratosphere. Rannou et al. (2003) investigated the coupling between haze microphysics and atmospheric dynamics. Latitudinal transport by the mean meridional circulation has been shown to produce a permanent accumulation of haze in polar regions. This excess in turn increases cooling to space at high latitudes, enforcing the mean meridional circulation, zonal wind and latitudinal temperature contrasts. The absence of coupling with the haze in H95 thus explains the major deficiencies of their 3D simulations (performed with a haze varying as a function of altitude only), with latitudinal variations of chemical species having a weaker impact on dynamics (Lebonnois et al., 2003).

In the 2D model, only the axisymmetric component of the circulation is accounted for explicitly and the latitudinal transport by non-axisymmetric waves must thus be parameterized. In early studies (in particular in that by Lebonnois et al., 2001) this transport was prescribed as a classical lateral eddy diffusion, with a diffusivity estimated from diagnostics of the 3D model and varying as a function of altitude only. In the present study a more physical parameterization is proposed, in which the intensity of the lateral mixing depends on the strength of the instability of the mean flow. It is based on the results of the shallow-water simulations of paper 1. With the new parameterization (which was already present in the studies by Lebonnois et al., 2003, and Rannou et al., 2003) the 2D GCM is able to reproduce satisfactorily the thermal structure, the dynamical regime and the latitudinal distribution of chemical species.

The GCM is briefly described in Section 2, while the adaptive parameterization of horizontal eddy-mixing is developed in Section 3. In Section 4 we analyze the GCM results focusing in particular on the impact of the parameterized mixing on the general circulation and on the latitudinal contrasts of trace species. Section 5 discusses the main results.

## 2. The latitude–altitude GCM

### 2.1. Axially-symmetric dynamics, radiative transfer and haze

The model is a 2-dimensional, latitude–altitude version of the 3D Titan GCM of H95. The vertical discretization consists of 55 levels, of which the last three serve as a sponge layer to damp down the wind and prevent spurious reflections of waves. Level 52 is at approximately 480 km. The vertical resolution is about 3 km in the troposphere, 5 km at the tropopause and 10–15 km in the stratosphere, which corresponds to one half to one third of a scale height. The numerical formulation is based on the shallow-atmosphere approximation, neglecting variations in planetary radius except when differentiated. Although this is perfectly justifiable for terrestrial GCMs (on Earth the pressure falls off to $\sim 10^{-3}$ of the surface value at less than 1% of the Earth's radius), for Titan the shallow-atmosphere approximation is a much poorer one (8% of the titanean radius). Ideally, future developments of Titan GCMs should take a "deep-atmosphere approach" and include in their formulation the variation of radius with height. The advection of haze and trace species is modeled with the finite-volume scheme of van Leer (1977) (see also Hourdin and Armengaud (1998) for validation in the terrestrial version of the GCM). The radiative transfer is computed with the model of Toon et al. (1989) for the solar range (UV to near IR) and of McKay et al. (1989) for the thermal IR part of the spectrum. The coupling with the haze is described in detail in Rannou et al. (2003). The fractal particles model of Cabane et al. (1992) is assumed for the haze. Ten size categories are considered for haze particles, with a mass ratio of 16 between adjacent sizes. This allows a correct representation of the geometric albedo, while keeping the computational load under control. The haze optical properties are based on the mean field theory of scattering by fractal aggregates of Botet et al. (1997) and applied by Rannou et al. (1997). Since the haze is carried by the wind, its visible and IR properties are computed in each grid cell.

### 2.2. Idealized photochemistry

Lebonnois et al. (2001) used a chemistry-transport model to simulate the latitudinal contrasts of trace species retrieved by Voyager 1 (Coustenis and Bézard, 1995). They forced a photochemical module (Toublanc et al., 1995) with a 2D latitude–altitude advection code in which the 2D circulation was prescribed according to GCM results. Their results approximately reproduced the retrieved composition at 2 mbar, which pointed to an important influence of stratospheric dynamics on the particular latitudinal contrasts of chemical species. This was demonstrated by reducing all the photochemistry to a simple model in which the chemical sources and sinks of a given compound were represented by a relaxation of the mixing ratio towards the mean vertical profile

extracted from the full 1D photochemical model. The concentrations obtained were very similar to those computed with the full model. Their main conclusion is that latitudinal contrasts arise from differential vertical transport in the atmosphere since, the photochemically-active layer being located in the upper mesosphere, concentrations of trace species increase strongly with height. Hence subsiding air enriches the stratosphere, whereas ascending air depletes it. We have included in the GCM the six species, $N_2$, $CH_4$, $H_2$, HCN, $C_2H_2$, and $C_2H_6$ of their "idealized tracers" model. The real photochemical balance between the sources and sinks of a given species $i$ is represented by a relaxation of its concentration $q_i(\phi, z, t)$ towards a vertical compositional profile $q_i^0(z)$. The source term $S_{q_i} = (q_i^0(z) - q_i(\phi, z, t))/\tau_i$ represents the rate of change of the concentration of an idealized tracer ($\phi$, $z$, and $t$ are, respectively, the latitude, height and time). Both the relaxation profiles $q_i^0$ and the time constants $\tau_i$ are prescribed according to Fig. 13 of Lebonnois et al. (2001).

## 3. Parameterizing barotropic waves in the GCM

Here we develop a parameterization of the transport of trace species, haze, temperature and angular momentum by barotropic waves in Titan's stratosphere. For the transport of trace species a mixing-length approach is retained as in Lebonnois et al. (2001), but the diffusivity is allowed to vary both vertically and latitudinally. For momentum, the formulation is based on a heuristic approach to the mixing of vorticity. Since the waves arise from barotropic instability of the mean flow, their effect is modeled as a function of the strength of the instability, with the function parameters being derived from a set of experiments with the shallow-water model (SWM) described in paper 1. As pointed out in that article, the SWM represents mid-latitude eddies but not the low latitude eddies that, in principle, should help to create equatorial superrotation. In that sense our parameterization for the mixing of trace species is in fact a generalization to all latitudes of mixing by the mid-latitude eddies actually represented in the SWM. This incompleteness will have to remain unsolved until a realistic 3D GCM explicitly representing all kinds of non-axisymmetric motions becomes available.

### 3.1. General formulation

In order to properly decompose the flow into an axisymmetric component plus eddies, one must use an air-mass-weighted zonal average $\tilde{q} = [\rho q]/[\rho]$ (where $[x]$ is the zonal average $[x] = \int_{-\pi}^{\pi} x \, d\lambda/2\pi$, and $\lambda$ is the longitude). If $\mathbf{v} = (u, v, w)$ is the wind velocity, then the continuity equation

$$\frac{\partial \rho}{\partial t} + \text{div}(\rho \mathbf{v}) = 0 \qquad (1)$$

remains unchanged when zonally averaged with $[\rho]$ and $\tilde{\mathbf{v}}$ replacing $\rho$ and $\mathbf{v}$. The non-axisymmetric component of a

given quantity $q$ is defined as $q^* = q - \tilde{q}$, with the property $[\rho q^*] = [\rho q] - [\rho]\tilde{q} = 0$. Then, considering the equation for a conserved quantity $q$:

$$\frac{\partial(\rho q)}{\partial t} + \text{div}(\rho \mathbf{v} q) = 0, \qquad (2)$$

the zonally-averaged flux can be decomposed as $[\rho \mathbf{v} q] = [\rho]\tilde{\mathbf{v}}\tilde{q} + [\rho \mathbf{v}^* q^*]$, so that the zonal average of Eq. (2) reads

$$\frac{\partial[\rho]\tilde{q}}{\partial t} + \text{div}([\rho]\tilde{\mathbf{v}}\tilde{q}) + \text{div}[\rho \mathbf{v}^* q^*] = 0. \qquad (3)$$

Our purpose is to parameterize the term $\text{div}[\rho \mathbf{v}^* q^*]$, i.e., to write it as a function of zonally-averaged flow without knowing the details of the actual perturbative 3D field. Noting that the zonal component of the divergence is zero then, considering only the latitudinal transport by eddies (vertical eddy transport was shown to be negligible in H95), the conservation equation of the 2D GCM can be written:

$$\frac{\partial(\rho q)}{\partial t} + \frac{1}{a \cos \phi} \frac{\partial}{\partial \phi}(\cos \phi \, \rho v q) + \frac{\partial(\rho w q)}{\partial z}$$
$$= [S_q] - \frac{1}{a \cos \phi} \frac{\partial}{\partial \phi}(\cos \phi[\rho v^* q^*]), \qquad (4)$$

where $a$ is Titan's radius and the notation [ ] and $\tilde{}$ has been dropped since $[\rho]$, $\tilde{\mathbf{v}}$ and $\tilde{q}$ are the explicit variables of the 2D GCM. The equation is valid for zonal angular momentum, potential temperature, chemical compounds and haze with different source terms $S_q$. For all these variables $S_q$ includes a term corresponding to vertical turbulent mixing plus a specific source term for potential temperature, chemical reactions and haze microphysics.

### 3.2. Mixing-length approach to the transport of trace species

Mixing-length theory, which is used extensively for parameterizing turbulent transport in the planetary boundary layer, is a classical approach to down-gradient transport. For trace species the rationale is that waves mix tracers by transporting air across latitude circles. In an atmosphere enriched at the north pole with a tracer southward winds ($v^* < 0$) advect enriched air ($q^* > 0$). Conversely, northward winds are associated with tracer-depleted air so that, in both cases, the associated transport term is southward ($\rho v^* q^* < 0$), down the concentration gradient. Given the mixing length $l$, a fluid element is assumed to be representative of conditions a distance $l$ upstream, and $q^* = \mp(l/a)\partial q/\partial \phi$, with the minus (plus) sign being associated to a positive (negative) fluctuation of the meridional wind field. Then the northward eddy-flux of tracer $q$ can be written

$$[\rho v^* q^*] = -\rho \frac{K}{a} \frac{\partial q}{\partial \phi}, \qquad (5)$$

where $K(\phi, t) = l v_{\text{eddy}}$ is the mixing coefficient or diffusivity, and $v_{\text{eddy}}$ is the typical intensity of the meridional eddy wind component $v^*$.

### 3.2.1. Computation of the mixing coefficient

We have used the tracer and wind fields of the SWM of paper 1 to derive the mixing coefficient. Since $v^*$ and $q^*$ are explicitly represented in the model, Eq. (5) has been used to compute $K$ from the averaged northward eddy fluxes. Figure 1 shows the results for the three tracers $q_1$, $q_2$, and $q_3$ shown in Fig. 7 of paper 1. The mixing coefficient differs only very slightly for the different tracers. This indicates that the form chosen for the parameterization is satisfactory, since it depends on the flow but not on the particular tracer profile. The shape of $K$ can be approximated by a Cauchy function, or resonance

$$\mathcal{K}(\phi) \equiv A \frac{(\Gamma/2)^2}{(\phi - \phi_0)^2 + (\Gamma/2)^2}, \qquad (6)$$

where $A$ is the amplitude, $\Gamma$ is the full width at half-maximum (FWHM) and $\phi_0$ is the center of the peak. This form yields a better fit than a gaussian (which has been used as a first trial), because it falls off less steeply with $\phi$ and therefore represents better the wings of the curve far from the center. Since the mixing coefficients obtained from the three independent tracers are approximately equal, a mean $\widetilde{K} = (K_1 + K_2 + K_3)/3$ is used. Figure 2 shows an example of $\widetilde{K}$ and the resulting fit with a Cauchy function. Its peak amplitude $\widetilde{K}_{\max} \simeq 3 \times 10^5 \ \mathrm{m^2 \, s^{-1}}$ approximately equals $l v_{\mathrm{eddy}} = a(\delta\phi/2)|v^*|$, which can be estimated from the horizontal wind field of the reference simulation of paper 1 with $\delta\phi \sim 30°$ and $|v^*| \sim 0.5 \ \mathrm{m \, s^{-1}}$.

### 3.2.2. Closure relation

The last step is to relate the parameters $A$, $\Gamma$, and $\phi_0$ to the mean zonal flow. For the amplitude this can be done through a parameter measuring the degree of barotropic instability of the flow and which can be explicitly computed in the model. We define this parameter as the integral of the PV gradient, $S_B$, in the region where it takes negative values

(the barotropically unstable region):

$$S_B = \int_{\phi_1}^{\phi_2} \frac{\partial[Z]}{\partial\phi} \, d\phi \qquad (7)$$

$$= [Z](\phi_2) - [Z](\phi_1), \qquad (8)$$

with $\partial[Z]/\partial\phi < 0$ between $\phi_1$ and $\phi_2$. In practice $S_B$ is always negative for unstable flow. As to the remaining parameters, the width and center of the unstable region can be written $W_B = \phi_2 - \phi_1$ and $C_B = (\phi_2 + \phi_1)/2$. They can also be related to $\Gamma$ and $\phi_0$ to characterize the instability.

### 3.2.3. Parameter fitting

In the SWM the zonal flow is relaxed towards a barotropically unstable profile (see Fig. 2 of paper 1), with a time constant $\tau_{\mathrm{rel}}$. The circulation at latitudes up to the jets is characterized by low vorticity and a rather homogeneous PV, and at high latitudes it is close to solid-body rotation. The relation between $(A, \Gamma, \phi_0)$ and $(S_B, W_B, C_B)$ has been determined from a set of experiments with varying $\tau_{\mathrm{rel}}$. This is equivalent to varying the degree of barotropic instability of the mean flow, with the shorter values of $\tau_{\mathrm{rel}}$ leading to more unstable mean profiles. The process can be summarized in the following steps:

(1) a simulation is run for each relaxation time constant, $\tau_{\mathrm{rel}}$, until a steady state is reached. The stop criterion is a negligible variation ($\sim 1\%$) of the peak zonal wind, requiring an integration time typically 4–6 times $\tau_{\mathrm{rel}}$;

(2) the coefficients $K_i$ ($i = 1, 2, 3$) are computed from Eq. (5) for the three zonally-averaged tracers $q_{1,2,3}$, and $\widetilde{K}$ is obtained. Parameters $(A, \Gamma, \phi_0)$ are subsequently computed from $\widetilde{K}$, by fitting it with a Cauchy function (Eq. (6));

(3) the parameters $(S_B, W_B, C_B)$ are computed from $[Z]$, $\phi_1$ and $\phi_2$;

(4) a correlation is sought between the $(A, \Gamma, \phi_0)$ and $(S_B, W_B, C_B)$ obtained from the set of experiments.
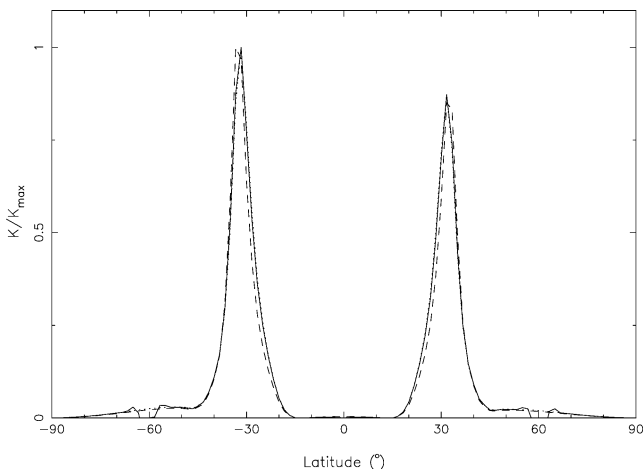


Fig. 1. The normalized mixing coefficients $K_1$, $K_2$, and $K_3$, computed from Eq. (5) for the three continuous tracers $q_1$ (solid line), $q_2$ (dashes), and $q_3$ (dots) introduced in paper 1.
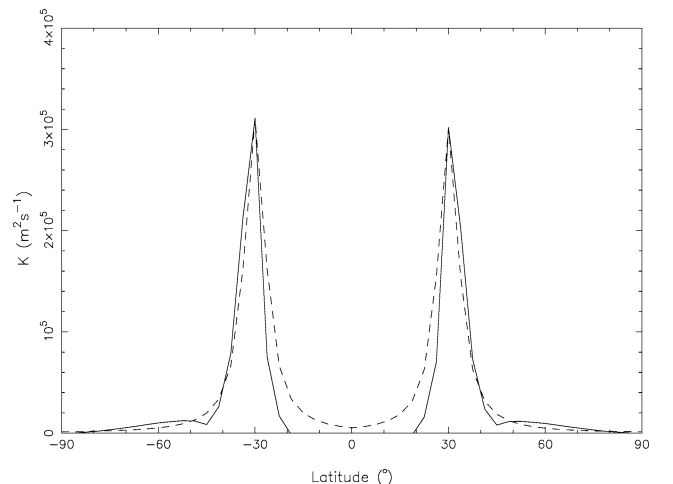


Fig. 2. The mixing coefficient retrieved from the profiles of $q$ and $v^*q^*$ in Fig. 7 of paper 1 (solid line, for ($\tau_{\mathrm{rel}} = 5$ d)) and the corresponding fit by a Cauchy function in each hemisphere (dashed).
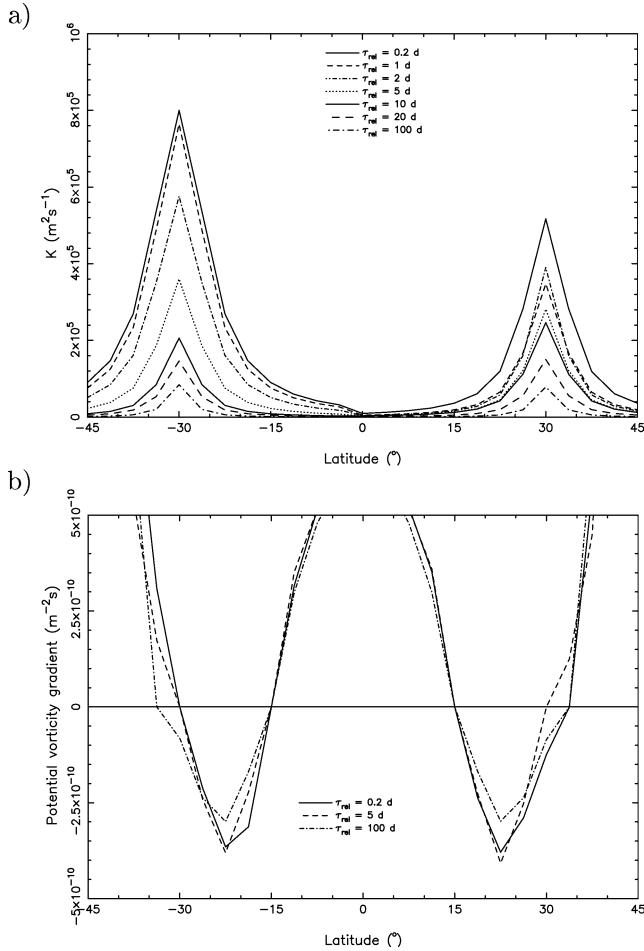
a)



b)



Fig. 3. The latitudinal profiles of the mixing coefficient for a set of experiments with varying relaxation time constants of the zonal wind: $\tau_{rel} = 0.2$, 1, 2, 5, 10, 20, and 100 Titan days (a) and 3 examples of the potential vorticity gradient (b). The results are for the reference model introduced in paper 1.

Based on the tests presented in paper 1, a resolution of $64 \times 48$ points has been used. Figure 3a shows results from seven experiments with $\tau_{rel}$ varying from 0.2 d to 100 d. Figure 3b shows the gradient of PV for three of the experiments (other curves are very similar). There is a clear spatial correlation between the center and width of the peaks and the barotropically unstable region. From the figure we take $\Gamma \simeq (\phi_2 - \phi_1)/2$ and, since the peak is centered on the poleward zero of the PV gradient, $\phi_0 \simeq \phi_2$ as approximations. Figure 4 shows the amplitude $A$ plotted against the strength of the instability, $S_B$. Each triangle-circle pair represents one simulation, with each cross representing the mean of the pair. The straight line is a least-squares linear fit of the mean points. Although the north–south difference increases with decreasing $\tau_{rel}$, the means are well correlated by the straight line. The fit yields an exponential relation

$$\log_{10} A = a - 10^{11} b S_B \tag{9}$$

with $a = 1.781$ and $b = 0.5928$. The narrow range of values of $S_B$ in Fig. 4, ranging from $-8 \times 10^{-11}$ to $-5 \times$
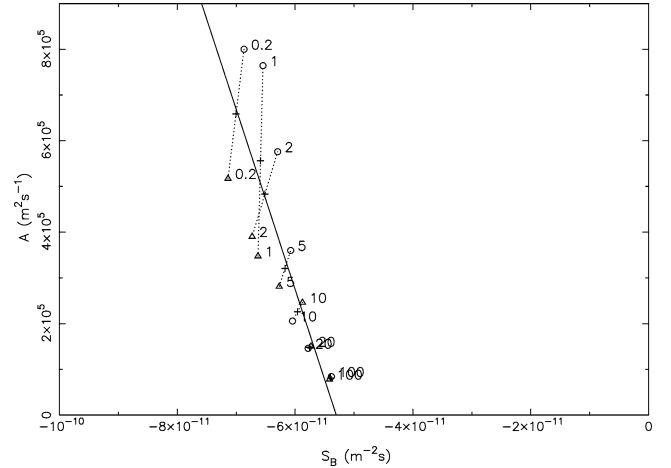


Fig. 4. The amplitude of the mixing coefficient versus the strength of the barotropic instability, obtained from the set of experiments in Fig. 3a. Circles and triangles connected with dotted lines respectively represent peaks in the southern and northern hemispheres obtained with the same value of $\tau_{rel}$. For each experiment a single point can be defined as the arithmetic mean of the amplitudes in the two hemispheres (crosses). The straight line is a least-squares fit to the set of mean points.

$10^{-11}$ m$^{-2}$ s, whilst $\tau_{rel}$ varies by some 3 orders of magnitude, is noteworthy. This behavior in which the mean flow is little sensitive to the forcing indicates that eddies keep the flow close to marginal stability, as discussed in paper 1.

### 3.3. Modeling the transport of angular momentum

Eddy fluxes of angular momentum have an important up-gradient component (paper 1) and thus cannot be represented by a diffusion of angular momentum. On the other hand, these fluxes amount to a mixing of potential vorticity leading to a decrease of the instability towards a neutrally-stable state (paper 1, Allison et al., 1994; Del Genio et al., 1993). To be consistent with these constraints, our parameterization for the transport of angular momentum is based on an approximate mixing of vorticity (we use vorticity rather than potential vorticity since the parameterization aims to represent barotropic mixing). Applied to relative vorticity (the result is the same for absolute vorticity)

$$\eta = -\frac{1}{a \cos \phi} \frac{\partial}{\partial \phi} (\cos \phi \, u) \tag{10}$$

a mixing-length approach gives

$$\frac{\partial \eta}{\partial t} = \frac{1}{a^2 \cos \phi} \frac{\partial}{\partial \phi} \left( \cos \phi \, K \frac{\partial \eta}{\partial \phi} \right), \tag{11}$$

where $\partial / \partial t$ is the acceleration due to eddy transport. Taking the time derivative of Eq. (10) and combining with (11) yields

$$\frac{\partial u}{\partial t} = -K/a \frac{\partial \eta}{\partial \phi}, \tag{12}$$

which gives a parameterization for the transport of zonal momentum based on the mixing of vorticity, with a form

similar to Eq. (5). A natural idea would be to apply this operator directly, using a $K$ coefficient varying with both latitude and altitude, depending on the instability of the flow, as for tracers. Despite important efforts in that direction, we never succeeded in obtaining a stable model with such a parameterization. We initially tried to tune $K$ in Eq. (12) in much the same way we did for the passive tracers in Section 3.2, but this approach was unsuccessful and plagued by numerical instabilities when implemented in the GCM.

Instead, we adopted a more robust parameterization, taking a restriction to the axisymmetric model of the operator classically used to handle the interaction between resolved and subgrid-scale motions (H95, paper 1, Lebonnois et al., 2001):

$$\left(\frac{\partial \mathbf{v}_H}{\partial t}\right)_{\text{diss}} = (-1)^{n_{\text{diss}}+1} \frac{1}{\tau_{\text{diss}}} (\delta y)^{2n_{\text{diss}}} \Delta^{n_{\text{diss}}} \mathbf{v}_H, \qquad (13)$$

where $\Delta$ represents the vector laplacian and $\mathbf{v}_H = (u, v)$. In the absence of forcing, the operator applied to the wind leads to a solid rotation wind profile, which is an *a priori* requirement for a parameterization of vorticity mixing by eddies. Another heuristic argument for using this operator is that with the simple laplacian ($n_{\text{diss}} = 1$), Eq. (12) with $K = \delta y^2/\tau_{\text{diss}}$ and Eq. (13) are equivalent for relative vorticity. For absolute vorticity, which is the fundamental quantity being mixed towards a uniform profile in latitude, the equivalence is only approximate, to a term of the order of $\Omega K/a$. As is traditionally done in such parameterizations, we reinforce the operator's action on the smaller scales by iterating it. $n_{\text{diss}} = 2$ gives satisfactory results compared to observations and to the 3D GCM.

Our approach to the transport of angular momentum is based on a tuning of $\tau_{\text{diss}}$ in order to match the effect of vorticity mixing by eddies. The procedure is the following:

(1) the SWM is run with a given $\tau_{\text{rel}}$ until balance is reached between the explicitly-resolved horizontal dynamics and the forcing by the relaxation terms. The mean flow is the result of the full horizontal dynamics. Let $S_B^{\text{dyn}}(\tau_{\text{rel}})$ be the degree of instability of this flow;

(2) a set of simulations are performed with the advective terms in the momentum equations (see Eqs. (3) and (4) of Sadourny, 1975) replaced by dissipation (Eq. (13)). These simulations correspond to axisymmetric flow because advection is absent and only the dissipation operator (13) is acting on the mean zonal wind. The time constant for dissipation is varied between simulations, until the mean flow matches $S_B^{\text{dyn}}(\tau_{\text{rel}})$. Let $\tau_{\text{diss}}^{\text{dyn}}(\tau_{\text{rel}})$ be the corresponding dissipation time constant;

(3) the preceding steps are repeated for different values of $\tau_{\text{rel}}$, until a relation is obtained between $\tau_{\text{diss}}^{\text{dyn}}$ and $S_B^{\text{dyn}}$.

We have conducted seven sets of experiments, four with the reference and three with the case B wind profiles of paper 1. Figure 5 shows the results for the reference case. The heavy solid line has been obtained by a least-squares fit of
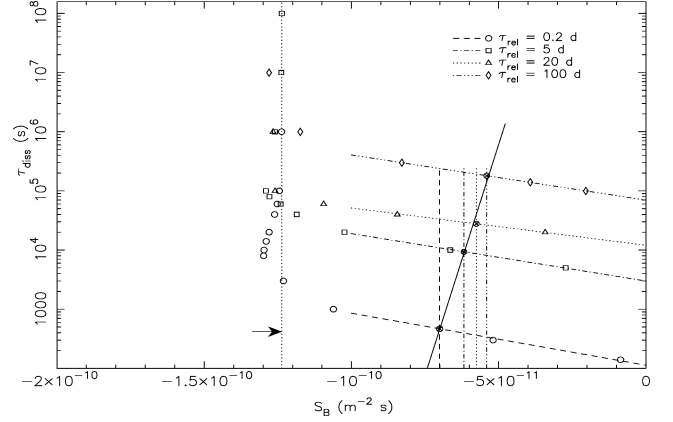


Fig. 5. The dissipation time constant $\tau_{\text{diss}}$ plotted against the degree of barotropic instability, $S_B$, for the set of experiments using the reference wind of paper 1. The value of $S_B^0$ (signaled by the arrow), corresponding to the relaxation profile, is the asymptote for the limit of no dissipation ($\tau_{\text{diss}} \to \infty$). Each set of open symbols (circles, squares, triangles and diamonds) corresponds to experiments using the same relaxation time constant $\tau_{\text{rel}}$. The vertical lines on the right represent $S_B^{\text{dyn}}$ obtained with the explicitly-resolved 2D dynamics (including eddies), for the simulations from step 1. Each point represents an experiment in which dissipation (Eq. (13)) replaces the advective terms (step 2). $S_B$ is computed from the steady state, zonally-averaged potential vorticity profile. The intersection ($\otimes$) of the curve for each set of points with the respective vertical line gives the value of $\tau_{\text{diss}}$ for which dissipation matches the effect of the full dynamics, $\tau_{\text{diss}}^{\text{dyn}}$. To find the intersections the last three points of each set were fitted with a least squares-line (oblique lines). The heavy solid line is a least-squares fit to the intersections, giving the variation of $\tau_{\text{diss}}^{\text{dyn}}$ with $S_B$.
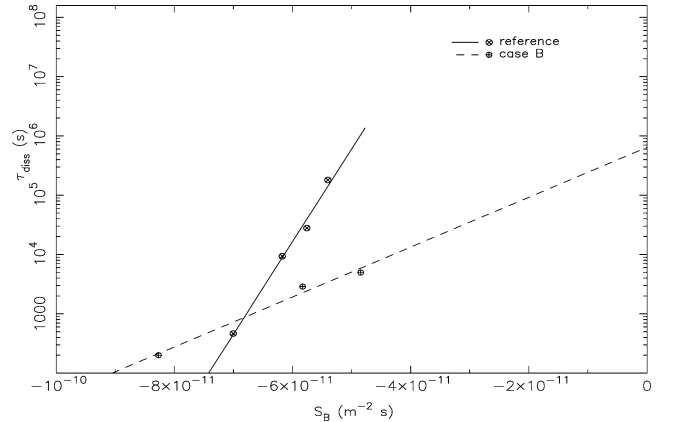


Fig. 6. The variation of $\tau_{\text{diss}}^{\text{dyn}}$ as a function of $S_B$ for the reference and case B wind profiles.

the pairs $(S_B^{\text{dyn}}, \tau_{\text{diss}}^{\text{dyn}})$, with

$$\log_{10} \tau_{\text{diss}}^{\text{dyn}} = c + 10^{11} d S_B^{\text{dyn}}. \qquad (14)$$

Figure 6 compares the results for both sets of experiments for the reference case and case B. The derived coefficients are $c = 13.59$ and $d = 1.562$ for the reference case, and $c = 5.81$ and $d = 0.4207$ for case B.

### 3.4. Numerical aspects

The parameterization has been implemented in the GCM, with the following procedure:

(1) negative latitudinal gradients of PV are searched for at each altitude level;

(2) the mixing coefficient and the time constant for horizontal dissipation are subsequently computed from Eqs. (6) and (14). While the mixing coefficient is computed for each level $z$ as a function of $\phi$, the time constant for the parameterized eddy-mixing of momentum depends on $z$ only. If the instability of the mean flow becomes large, Eqs. (9) and (14) may lead to too large a mixing coefficient or too strong a dissipation, which may cause numerical instabilities if the time step is kept constant. For this reason the amplitude of $\mathcal{K}$ for tracers is limited in the model to $A = 3 \times 10^6$ m$^2$ s$^{-1}$ and a lower bound $\tau_{\mathrm{diss}} = 5 \times 10^3$ s is imposed on $\tau_{\mathrm{diss}}$ for the wind. These bounds can be safely used with a dissipation time step of $\sim 700$ s;

(3) The values $\mathcal{K}(\phi, z)$ and $\tau_{\mathrm{diss}}(z)$ obtained from steps (1) and (2) are used to compute the parameterized transport by barotropic waves of trace species, aerosols and temperature (Eqs. (4) and (5)), and momentum (Eq. (13)). The implementation of the procedure in the 2D GCM allows for multiple $(i = 1, \ldots, N)$ regions of barotropic instability to occur, in which case one $K_i(\phi)$ is computed for each of them. The $K_i$ are then added and finally $\partial(\rho q)/\partial t$ is computed with $K = K_1 + \cdots + K_N$. The mixing is not constrained to only one region, but occurs in different regions with different intensities.

Figures 7a–7c compare results from the SWM (including the full dynamics), with results from the parameterized GCM. The GCM (dashed lines) approximately reproduces the full 2D dynamics (solid lines). The agreement is better for the larger relaxation time constant $\tau_{\mathrm{rel}} = 100$ d (right). Although the parameterized GCM does not exactly match the profiles obtained with the full 2D dynamics, it gives the same value for $S_B$, as expected.

## 4. Results of the 2D GCM

Our run represents a simulation of Titan's atmosphere for a period of 13 Titan years. For the atmospheric dynamics, a time step of about 140 s has been used in each iteration. Due to the longer time constants involved in dissipation, radiative balance/aerosol microphysics, and chemistry, these processes were performed only each 5, 1000, and 10000 iterations, respectively. The aerosols are coupled to the dynamics and are radiatively active. The artificial chemical tracers described in Section 2.2 are also advected, but are not active, i.e., the radiative balance is computed with a constant and uniform gas composition taken from McKay et al. (1989). This is not important, since Lebonnois et al. (2003) have shown that the coupling with chemistry has only a secondary impact on dynamics. Eddy mixing is computed with
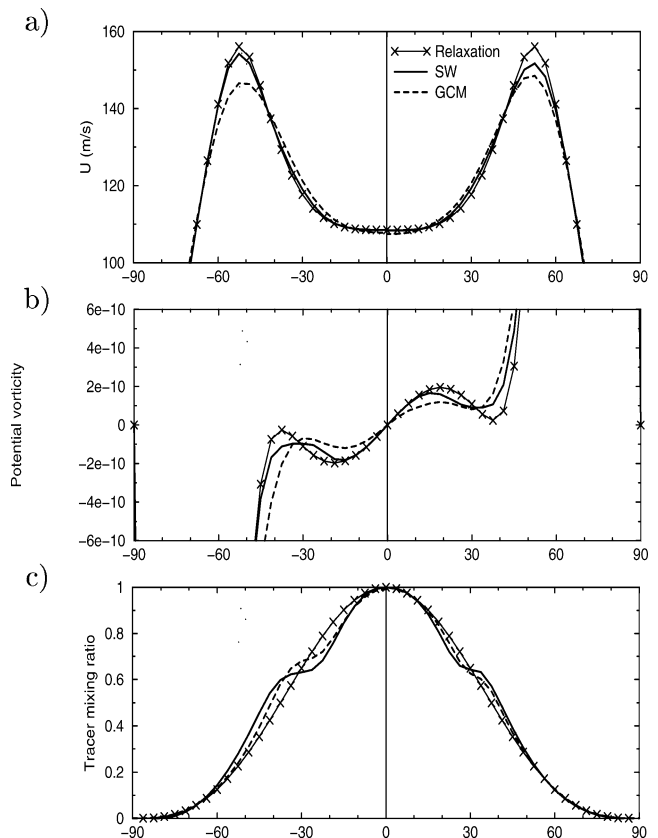


Fig. 7. A comparison of results from the shallow-water model with the full 2D dynamics (SW), and from the parameterized GCM. (a) Zonal wind; (b) vorticity; and (c) tracer 3 mixing ratio. The curves in the southern and northern hemispheres correspond to experiments with relaxation time constants $\tau_{\mathrm{rel}} = 10$ d and $\tau_{\mathrm{rel}} = 100$ d, respectively. The reference wind profile has been used for the forcing. The relaxation profile is also shown for comparison.

the adaptive parameterization of Section 3. The model was started from a state already in prograde superrotation which resulted from previous simulations. Note that although theoretical arguments (Flasar and Conrath, 1992), observational data (Kostiuk et al., 2001) and modeling results (Del Genio et al., 1993; Hourdin et al., 1995) strongly suggest that is the case, there is as yet no definite confirmation that the atmospheric spin is prograde.

### 4.1. General circulation

Figure 8 shows the averaged meridional mass streamfunction for northern winter solstice and spring equinox. A negative mass flux (grey areas) corresponds to a mean meridional flow with upwelling in the northern branch and subsidence in the southern. The circulation changes seasonally following the point of maximum insolation. The global circulation in the upper stratosphere and mesosphere is dominated by two large, thermally direct cells at equinoxes and by one large cell extending from pole to pole at solstices. At northern winter solstice air rises in the southern hemisphere and descends in the northern one, while at equinox
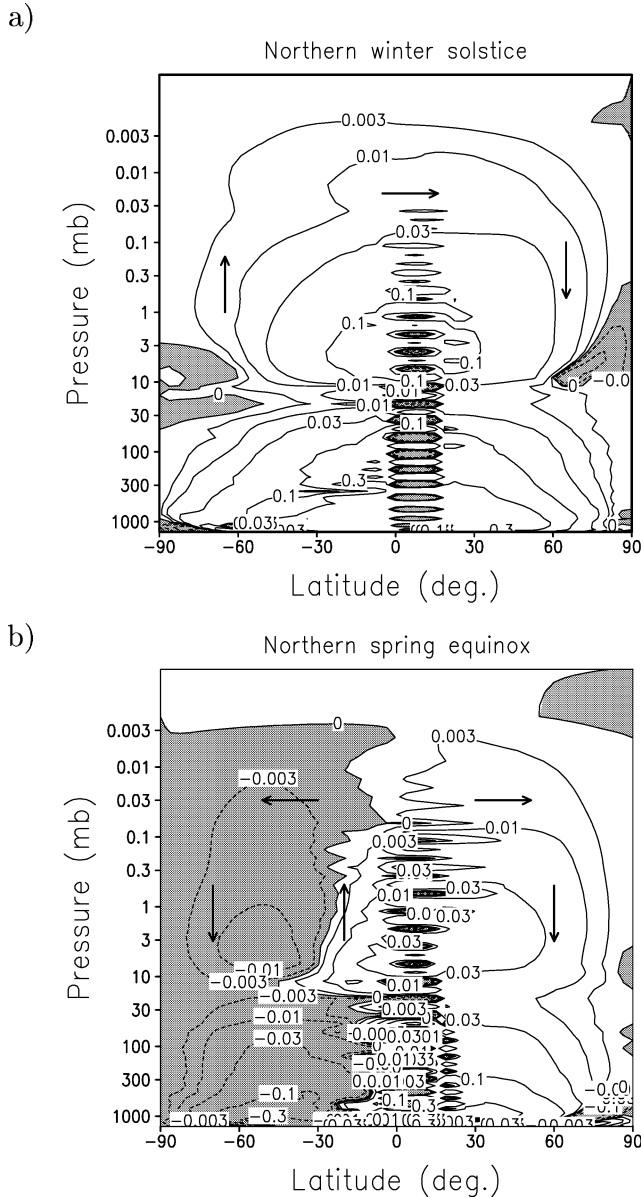
a)



b)



Fig. 8. The mass streamfunction of the mean meridional circulation ($\times 10^9$ kg s$^{-1}$) obtained from the control experiment for northern winter solstice (a) and spring equinox (b). The difference between contours equals the total mass flux. Negative contours, corresponding to southward motion in the upper branch, are shaded in grey. The panels show seasonal averages centered at solstice and equinox.

upwelling sets in at the equatorial region and downwelling occurs at both poles. The solstitial circulation covers most of the year, with the equinox corresponding to a short transition between two opposing pole-to-pole circulations. There is also a clear distinction between the circulation above and below the 30 mbar level, where the streamlines close. Above this level the solstitial circulation consists of one cell extending from the summer to the winter pole. The mass flux exhibits a series of vertical oscillations at equatorial latitudes, extending some 15° into the winter hemisphere. This layered structure has a physical basis that corresponds to

inertial instability at the tropics caused by the strong winter jet. Similar structures associated with inertial instability have been observed in the Earth's atmosphere and in terrestrial 3D-GCM results (Hitchman et al., 1987; Hunt, 1981), and were also present in the 3D GCM of H95, although not apparent from their figures. The criterion for the inertial instability is that $(f + 2[u] \tan \phi / a)[\eta] < 0$, where $f$ is the Coriolis parameter, $\eta = f - \partial[u]/\partial y + [u] \tan \phi / a$ is the absolute vorticity and $\partial[u]/\partial y$ is the latitudinal shear of the mean zonal wind. We computed this for model winds (not shown), which revealed inertially unstable flow at winter in the northern hemisphere, coincident with the layered structure. This is expected, since at low latitudes and for sufficiently strong winds the shear term dominates. The fact that the model lacks one dimension is, in principle, no impediment, since inertially unstable modes may develop under axisymmetric conditions (e.g., Andrews et al., 1987, p. 338). If the wind shear is comparable to that in the model, stationary layered flow will be a feature to look for at low latitudes in Titan's atmosphere. However, we also acknowledge that inertial instability is known to occur spuriously in 2D models. This is a question that merits further investigation.

Figure 9 shows the latitude–altitude charts of zonal wind (contours) and temperature anomaly (shaded, defined as the difference between the temperature and its latitudinal average). The winter zonal circulation consists of a strong jet centered at approximately 60° and 1 mbar, where the peak wind speed exceeds 140 m s$^{-1}$, with a much slower wind in the summer hemisphere. At equinox the hemisphere coming out of winter still has its jet almost unaltered, whilst the jet in the southern hemisphere has began to grow, fed by the larger supply of angular momentum by the augmented southern cell. The temperature anomaly is largest ($\sim 30$ K) at the winter pole at solstice and at both poles at equinox. The model reproduces the H95 inversion of the latitudinal temperature gradient above 1 mbar, which they pointed out is produced by the explicitly resolved dynamics since it was not present in purely radiative-convective simulations. Our results confirm that it is also independent of the haze-dynamics coupling.

Figure 10 shows the annually-averaged vertical profiles of the three wind components. The wind increases strongly with altitude, particularly above 30 mbar. Seasonal variations (not shown) correspond to an increase of the order of a factor 3 from equinox to solstice. Over the lowest scale height $v \sim 10^{-3}$ m s$^{-1}$, and $w$ is a factor 10 smaller, with both components being about 30 times larger at 1 mbar. In the upper stratosphere $v \sim 0.1$ m s$^{-1}$. These values are somewhat higher than early estimates by Flasar et al. (1981) and Flasar and Conrath (1990) ($v \sim 4 \times 10^{-4}$ m s$^{-1}$ and 0.05 m s$^{-1}$ respectively in the lower and upper stratosphere) based on the assumption of equilibrium between the equator-to-pole heat transport by the mean meridional circulation (MMC) and the forcing by solar radiation. This is due to our enhanced circulation, which arises from the coupling with the haze (Rannou et al., 2003).
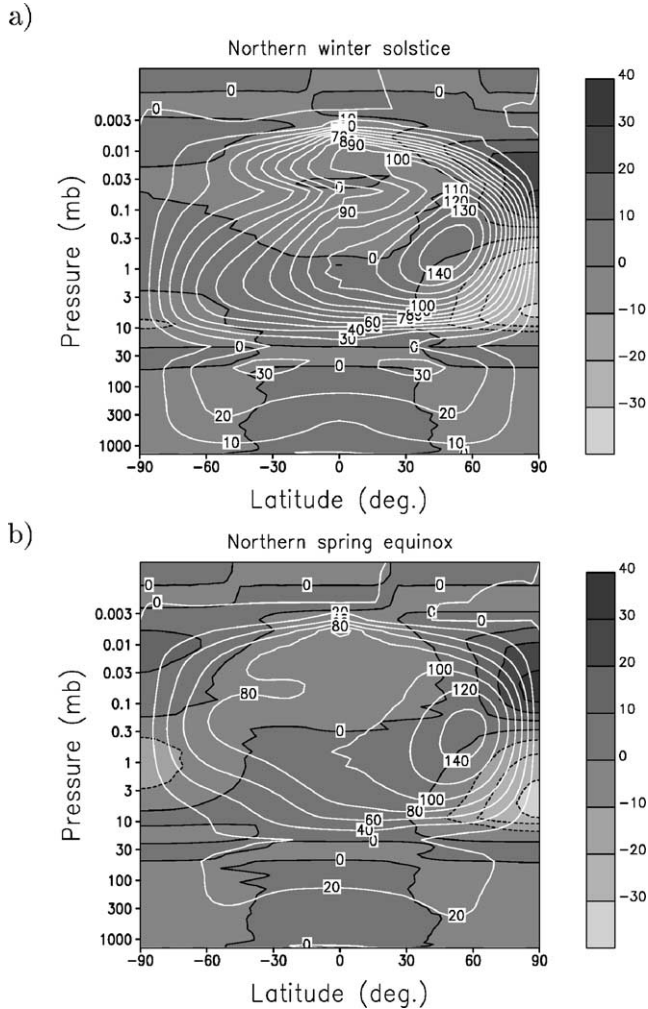
Northern winter solstice

Northern spring equinox



Fig. 9. The mean wind (contours, in m s$^{-1}$) and temperature anomaly (shades of grey, in kelvins, defined as the difference between the temperature and its latitudinal average) for the seasons centered at northern winter solstice (a) and spring equinox (b).
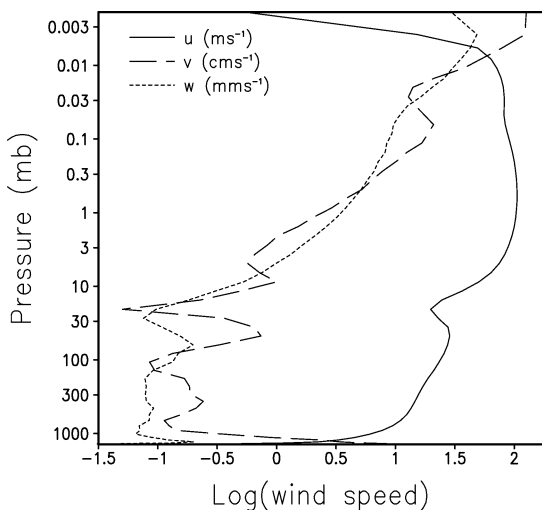


Fig. 10. Vertical profiles of the annually-averaged root-mean-square of the three wind components. Note the different units used.

The vertical temperature profile is shown in Fig. 11 (dashed line), for $\phi = 0°$ at $L_s = 9°$ (the solar longitude corresponding to the Voyager 1 flyby, shortly after northern spring equinox). It is compared with the profile derived by Lellouch et al. (1989) (solid line), and with the Voyager IRIS measurements at 0.4 and 1 mbar. Up to ∼ 0.25 mbar the model temperatures are close to the Lellouch et al. (1989) profile, with the model being colder by about 10 K in the tropopause and 6 K close to 4 mbar. However, the distribution of ethane in the low stratosphere (Lebonnois et al., 2003) or the height of the haze production layer Rannou et al. (2003) may affect the model temperature. Above 0.4 mbar the model becomes much warmer than the temperature proposed in previous studies (Lellouch et al., 1983, 1989; Yelle, 1991). The non-LTE model described in Yelle (1991) shows that non-LTE effects should be taken into account above ∼ $10^{-2}$ mbar. They also point out the strong effect of aerosol heating on the temperature above 300 km. Although direct observational constraints are scarce, the misrepresentation of the temperature profile at these heights clearly suggests the need for a better understanding of the radiative budget of the upper stratosphere.

The buoyancy frequency (Fig. 11) is greater than $3 \times 10^{-3}$ s$^{-1}$ everywhere up to 0.1 mbar, except in the lowest few kilometers. This high static stability confirms the assumption made in paper 1 that the flow is mainly horizontal. $N$ peaks at 30 mbar (a few km above the tropopause), reaching a value $\simeq 9 \times 10^{-3}$ s$^{-1}$ there. The vertical profile is in good agreement with Flasar (1998b). $N$ is a factor of 3 to 10 (at the tropopause) smaller than the result of the radiative-convective simulation of H95, which is probably due to the coupling with the haze and the resulting enhanced circulation in our model, which reduces the vertical potential temperature gradient.

### 4.2. Comparison with observations

Figures 12a and 12b show a comparison of model results with the Voyager 1 temperatures (Coustenis and Bézard, 1995; Flasar and Conrath, 1990) and with the wind derived from the stellar occultation (Hubbard et al., 1993). The model reasonably represents the observations for latitudes below 30°, with differences of less than 5 K for most points. However, it is some 5 K warmer than the observations above 30°, underestimating the latitudinal asymmetry. Although the uncertainties in the retrieved temperatures are high (illustrated by the disparities between the results of Coustenis and Bézard (1995) and Flasar and Conrath (1990), which are larger than the respective error bars due to the use of different procedures), the asymmetry in the IRIS data seems real and its representation by the model should be improved in the future. The IRIS observations probed a transition level in the vertical temperature gradient. The asymmetry is better represented in the GCM close to 0.1 and 3 mbar, which probably indicates a misrepresentation of the opacity due to the uncertainty in the height of
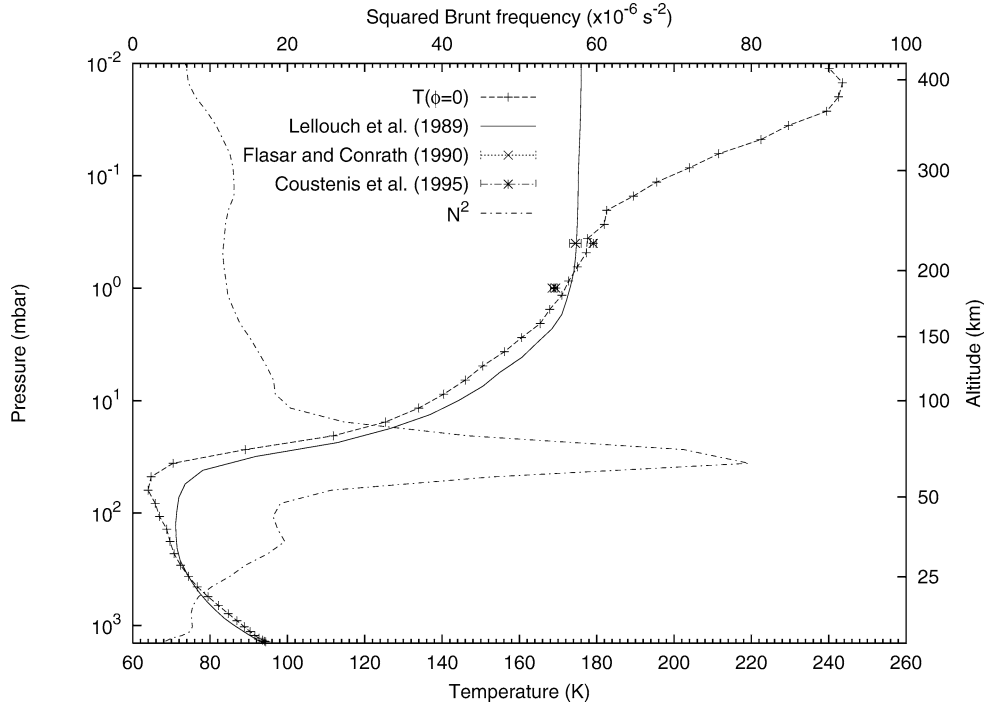
Fig. 11. The model vertical temperature profile at the equator at the time of the Voyager 1 flyby. The nominal profile derived by Lellouch et al. (1989) and the IRIS measurements of Coustenis and Bézard (1995) and Flasar and Conrath (1990) at 0.4 and 1 mbar are shown for comparison. The squared buoyancy frequency $N^2$ is also shown.

the haze production layer or the fact that the gas opacity is computed with a fixed distribution of ethane and other trace species.

The model (circles in Fig. 12b) also reproduces approximately the zonal jet at the epoch of the occultation (which occurred when Titan was at a solar longitude $L_s = 107°$, shortly after northern summer solstice), and the wind speed at $-20°$. It also compares well with the results shown in Fig. 9 of H95, albeit a somewhat better contrast is obtained here. The shaded area represents the latitudes which were accessible during the occultation. Latitudes poleward of $\pm 65°$ were not sampled because the north pole was tilted toward Earth, and latitudes north of $-20°$ contributed little because of the larger haze obscuration in the northern hemisphere (Flasar, 1998b). The oscillations in the retrieved wind speed are due to the use of a small number of Legendre polynomials in fitting the data to a iso-density height curve. The Hubbard et al. wind was obtained under the assumption of constant temperature along the 0.25 mbar isobar. Figure 9 supports the assumption of smaller temperature variations at 0.25 mbar than at 0.4 and 1 mbar, but this requires further investigation, since it is a transition region which may be sensitive to model parameters. On the other hand, the model wind also suggests that the assumption of symmetry relative to the equator used in the retrieval process was inadequate. In its region of validity, what can be inferred from the occultation profile is that there is a strong equatorial rotation, of $\sim 100$ m s$^{-1}$, and the existence of a high-latitude jet of $\sim 180$ m s$^{-1}$, with an intense equator-to-pole wind gradient.

### 4.3. Angular momentum balance

Figure 13a shows the isocontours of angular momentum and the streamlines of the meridional circulation in the stratosphere for northern winter solstice. The barotropically unstable regions, where the absolute potential vorticity gradient is negative (Charney and Stern, 1962), are shaded in the background. Figure 13b displays the acceleration of the zonal wind by the MMC (contours) and the parameterized latitudinal transport of zonal momentum by eddies ($v^*u^*$, shaded). Positive values correspond to northward momentum transport. Similarly to H95 the flow in the winter jet is barotropically unstable close to 1 mbar ($\sim 200$ km) and $20°$ latitude. At this altitude the latitudinal profile of angular momentum is rather flat between $-10°$ and $50°$, which favors the generation of the instability. Another unstable region occurs in the southern hemisphere above 1 mbar. The generation of the unstable regions can be interpreted in terms of the transport of angular momentum by the MMC. In the superrotating atmosphere momentum increases with altitude and poleward. Under inviscid conditions the streamlines of the zonally-averaged circulation are parallel to the contours of constant angular momentum. Figure 13a shows that this is not the case at solstice. Subsiding momentum-rich air in the winter hemisphere accelerates the zonal wind at high latitudes, increasing the wind shear and feeding the instability on the equatorward flank of the jet. Similarly, the MMC brings air from momentum-poor high latitudes, deep in the southern hemisphere, into the low latitudes, and a significant deceleration is produced there. This deceleration
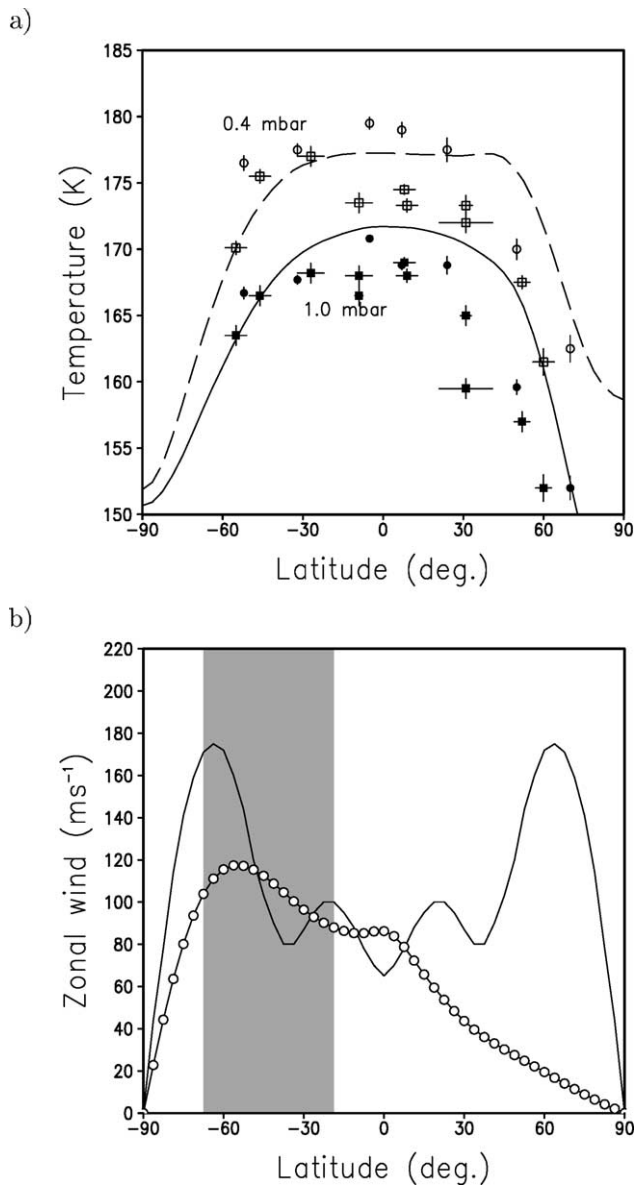
a)



b)



Fig. 12. A comparison of model results with the observations. (a) The Coustenis and Bézard (1995) temperature data at 0.4 mbar (open circles) and 1 mbar (closed circles) and the model temperatures at the same levels (dashed and solid lines, respectively) and season. The data retrieved by Flasar and Conrath (1990) are also shown (squares) for comparison. (b) The zonal wind speed retrieved by Hubbard et al. (1993) at approximately 0.25 mbar (solid line) and the wind from the GCM (circles) at the same epoch, close to northern summer solstice ($L_s = 107°$). The points in the wind profile illustrate the latitudinal discretization of the model.
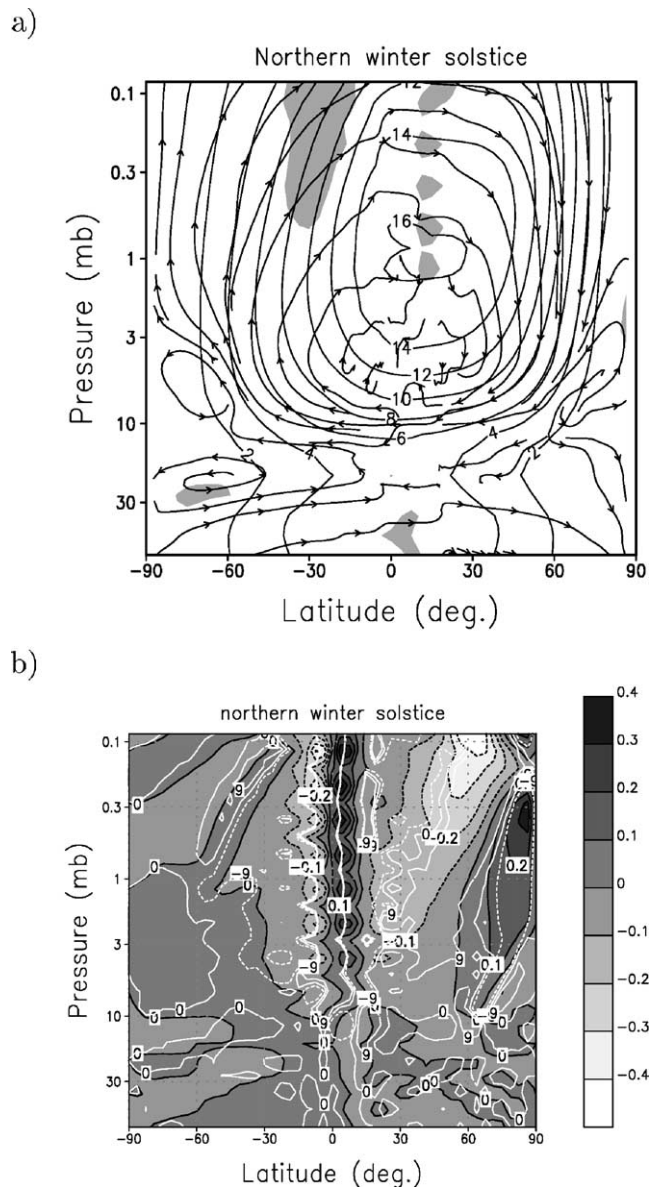
a)



b)



Fig. 13. (a) Seasonal average of the normalized angular momentum (heavy contours) and streamlines of the mean meridional circulation. Regions of barotropic instability are shown in grey. (b) Average of the parameterized latitudinal transport of zonal momentum by eddies, $v^*u^*$ (in $m^2\,s^{-2}$, shaded), and of the zonal acceleration by the MMC (in $m\,s^{-2}$, contours). Positive (negative) values of $v^*u^*$ correspond to northward (southward) transport.

causes the instability in the summer hemisphere (Fig. 15a). The combined effect of the parameterized eddy-momentum transport and the MMC is an enrichment with momentum of the barotropically unstable region, between 15° and 30° (Fig. 13b). This agrees with the results of paper 1 and other numerical models (Hourdin et al., 1992, 1995; Del Genio et al., 1993), and is the principle underlying the Gierasch mechanism for the maintenance of superrotation (Gierasch, 1975).

Seasonal changes are illustrated in Fig. 14, which shows the parameterized latitudinal momentum transport by eddies ($v^*u^*$, contours) and the zonal wind (shaded), at 0.25 mbar over one Titan year. The MMC builds the jet efficiently, which reaches a maximum shortly after autumn equinox ($L_s = -180°$ in the northern hemisphere). Eddy mixing simultaneously sets in between 30 and 60°, leading to an equatorward (negative) momentum transport which depletes the jet from northern winter solstice until shortly before the spring equinox. This corresponds to the wind gap between $L_s = -90°$ and 0°. The gap is more pronounced at higher
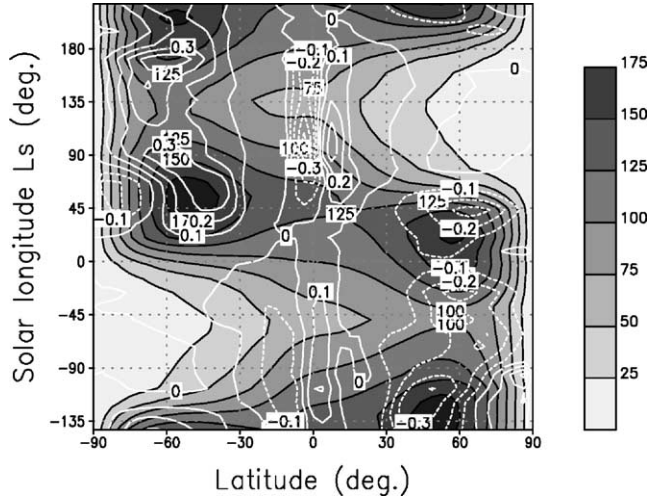
Fig. 14. Time evolution of the zonal wind (in m s$^{-1}$, shaded) and latitudinal transport of zonal momentum by eddies ($v^*u^*$, contours) at 0.25 mbar. $L_s = 0°$ corresponds to northern spring equinox.

altitudes, where mixing is stronger. Concomitantly with jet depletion, poleward transport occurs at low latitudes. The net effect is the transport of momentum into the barotropically unstable region. The rapid construction of the jet in early winter is consistent with a short time scale for the forcing of the zonal wind by the MMC, which we assumed in paper 1 to be of the order of 5 Titan days, based on H95.

### 4.4. Eddy-mixing time scale from the parameterized transport

Figure 15 helps to understand how the parameterized mixing is related to the flow. It shows the regions of barotropically unstable flow and the mixing coefficient, $K$, from 10 to 10$^{-3}$ mbar at northern winter solstice (a), spring equinox (c), and for a 20-day average before equinox (b). Panel b is a sample of the mixing that determines equinoctial conditions (the state seen by Voyager). The dominant features are a mixing region upward of 3 mbar at 20°, which persists from solstice to equinox, and an important mixing in the summer hemisphere (panel a). At equinox mixing occurs mainly in the upper stratosphere. The correlation between $K$ and the gradient of PV is a direct consequence of the formulation of the parameterization (Section 3): the vertical variation of $K$ coincides with that of the PV gradient, and its latitudinal variation is such that it peaks at the poleward flank of the barotropically unstable region (Fig. 3).

Figure 16a shows the averaged vertical profile of $K$ for the four northern seasons. Above 3 mbar the strength of the mixing changes by about one order of magnitude between equinox and the following solstice. The increase is due to the generation of barotropically unstable flow on the equatorward flank of the winter jet and in the summer hemisphere. Below 10 mbar the effect is negligible. The typical time scale for eddy mixing, $\tau_{\text{eddy}} \sim (a\delta\phi/2)^2/K$, can be estimated from $K$ by assuming a spatial scale for the eddies.
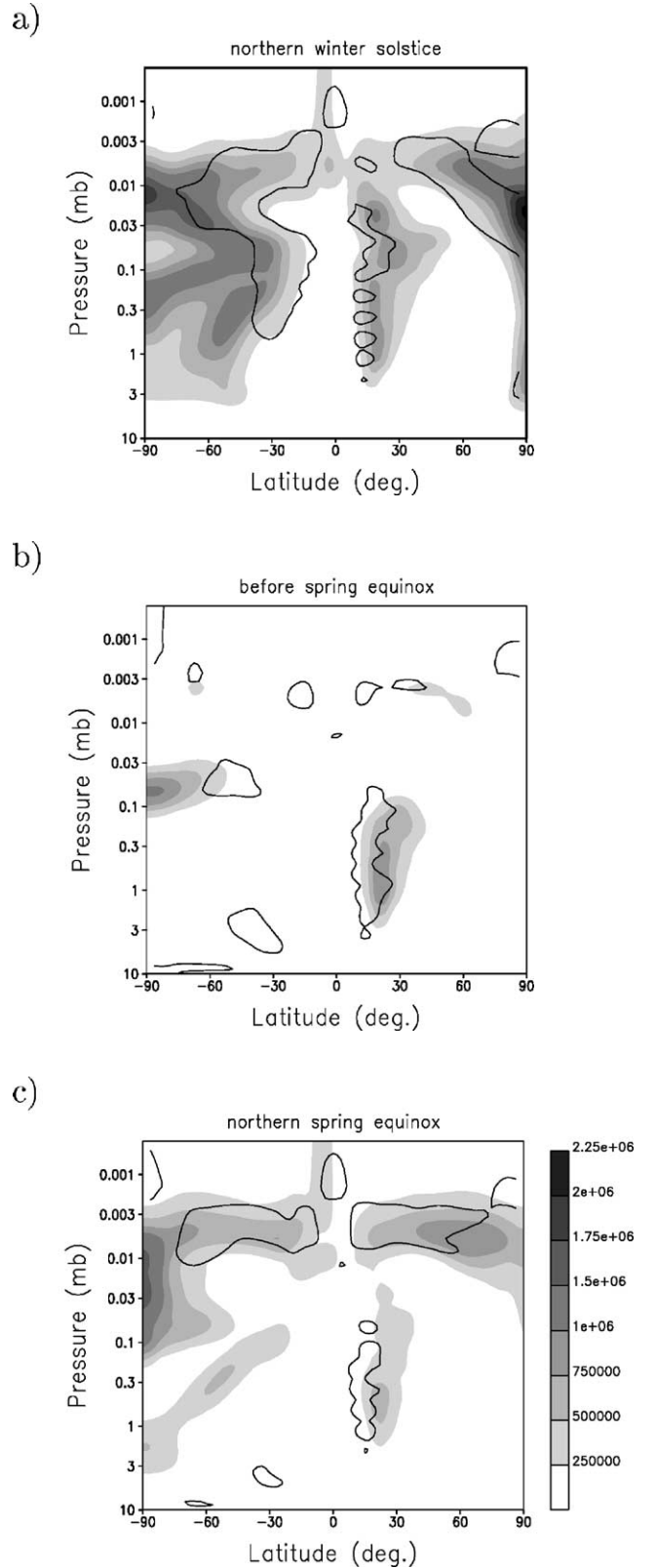
a)



b)



c)



Fig. 15. The mixing coefficient $K$ (shaded) at northern winter solstice (a), spring equinox (c) and for a 20-day average shortly before spring equinox (b). The solid contours enclose regions of barotropically unstable flow (negative gradient of absolute potential vorticity).
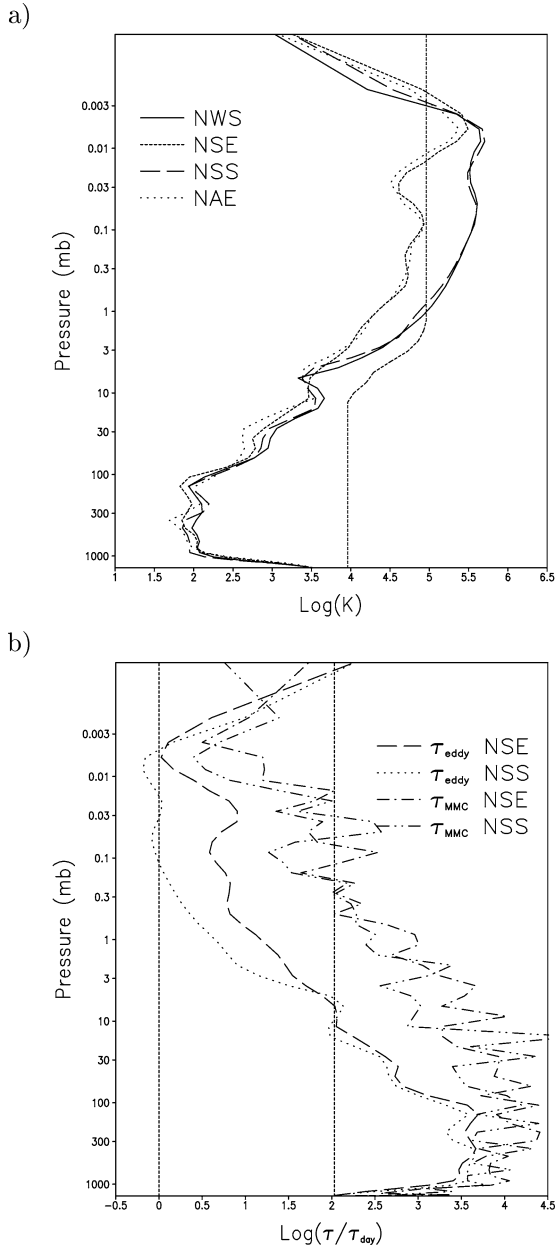
a)



b)



Fig. 16. (a) The latitudinally averaged mixing coefficient for the four northern seasons. The vertical dashed line corresponds to the model of fixed dissipation (Lebonnois et al., 2001). The transition around 5 mbar is due to the use of different dissipation time constants for the troposphere and stratosphere. (b) The time scale for eddy mixing ($\tau_{eddy} = (a\delta\phi/2)^2/K$, with $\delta\phi \sim 30°$ and $K$ averaged in latitude) and for mixing by the mean meridional circulation ($\tau_{MMC} = a/v$) for northern spring equinox and summer solstice. The two vertical lines represent the Titan day and the seasonal time scale (= 1 Titan year/$2\pi$).

Figure 16b shows $\tau_{eddy}$ compared with the dynamical time constant for the MMC, $\tau_{MMC} = a/v$, in Titan days. Based on paper 1, a spatial scale $\delta\phi = 30°$ is assumed. The two vertical lines represent the Titan day and the seasonal time scale (= Titan year/$2\pi$). Over the lowest scale height, typically $a/v \sim 2000$ d. This amounts to a mean meridional wind $v \sim 10^{-3}$ m s$^{-1}$. At the 2 mbar level $\tau_{eddy}$ varies from a few

days at solstice to tens of days at equinox, and increases with depth. It is always smaller than the typical time constant for advection by the MMC, which at this level is close to one year. The latitudinal average in Fig. 16 hides strong latitudinal contrasts, which are clearly apparent from Fig. 15. Under solstitial conditions meridional transport is dominated by non-axisymmetric processes which tend to erase latitudinal contrasts in less than a season, with the more intense mixing occurring in the summer hemisphere and in the equatorial flank of the winter jet (Fig. 15a). At equinoxes, however, eddy mixing is non-negligible only at the flank of the jet (Fig. 15c), and the typical time scale for the MMC is still longer than the seasonal time scale. The absence of mixing mechanisms away from the flank of the jet thus contributes to the persistence at spring of the latitudinal contrasts developed during winter.

## 4.5. Trace atmospheric components

Figure 17 shows the distributions of the idealized species HCN for northern winter solstice and spring equinox. The shaded contours in the background represent an average of $K$ for the 20 preceding days. Figure 18 compares model results at 2 mbar with the chemical profiles retrieved by Voyager 1 for HCN and $C_2H_2$. In both the full photochemical model and the idealized-tracers model described in Lebonnois et al. (2001), the absolute value of the equatorial mole fraction of each species differs from the abundances retrieved. This is also the case in the present simulation. Since our main interest is to represent the latitudinal contrasts, we have multiplied the distributions by normalizing factors in order to fit the equator (mean of the two observational data at $\pm 7°$). These factors reflect the differences between our absolute baseline profiles and the data. The difference is due to the particular photochemistry of Titan, which is not represented in the simple idealized tracers model. Lebonnois et al. (2001) identified the MMC, associated to the vertical concentration gradient of the trace species, to be the cause of the latitudinal gradients observed: in the winter hemisphere, subsiding air coming from tracer-rich altitudes increases the tracer content in stratospheric levels. The opposite occurs in the summer hemisphere, with tracer-poor air coming from deeper levels depleting the stratosphere. This can be seen in Fig. 18 for the trace species at northern winter solstice (dashed lines). Simultaneously, our results show that this contrast is reinforced by the effect of eddy-mixing: Fig. 17 shows a striking correspondence between regions where the tracer is homogeneous and regions that had strong mixing shortly before. Particularly at solstice it is clear that the parameterized eddy-mixing tends to homogenize the tracers at the flank of the winter jet, while preserving the contrasts at the higher latitudes. This can be compared to the effect of polar vortex isolation observed in the Antarctic, which may also occur on Titan (Flasar, 1998a). During winter the intense potential vorticity gradient at high latitudes, in the vicinity of the stratospheric jet, acts as a barrier preventing
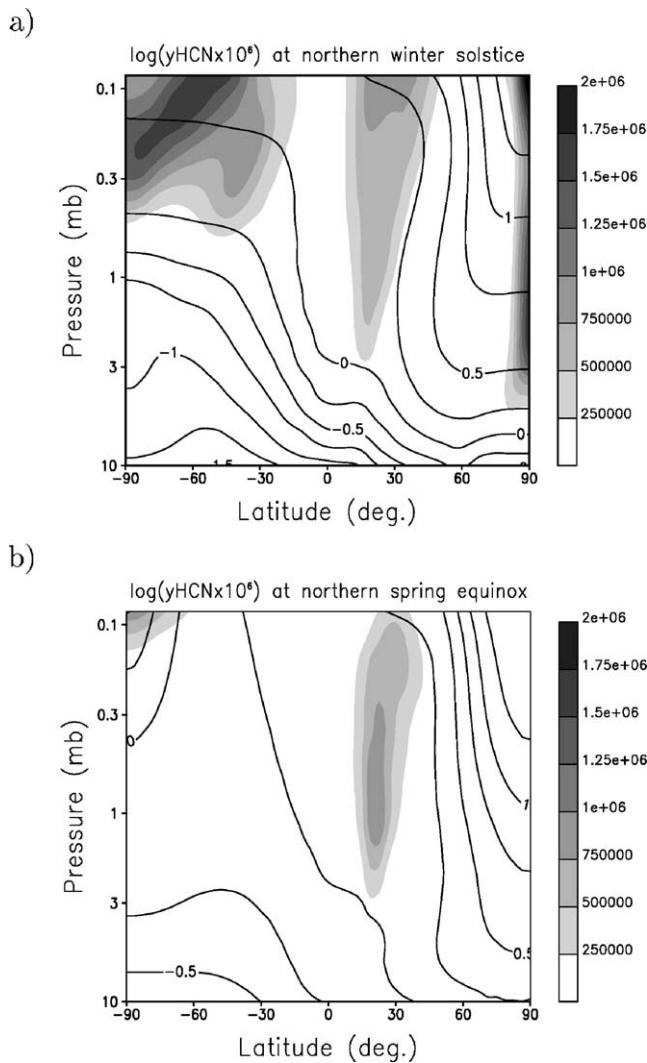
a)



b)



Fig. 17. Logarithmic contours of the atmospheric abundances of trace species, in ppm ($10^{-6}$ kg kg$^{-1}$ of air). The mean mixing coefficient $K$ is shown in shades of grey for the 20 days preceding solstice and equinox.

a)



b)



Fig. 18. A comparison of model results at 2 mbar at the time of the Voyager 1 flyby ($L_s = 9°$, solid lines) with the abundances retrieved from IRIS measurements (Coustenis and Bézard, 1995) for HCN and $C_2H_2$. Dashed lines represent model results for northern winter solstice. The curves have been normalized by factors such that at the equator the curve for Voyager equals the mean of the data at $-7°$ and $7°$. The normalizing factors are 0.193 for HCN and 1.36 for $C_2H_2$.

the mixing of air coming from low latitudes with polar air. By mid-spring planetary waves start to erode the vortex and to mix air across the edge (Schoeberl and Hartmann, 1991). Our results support this hypothesis. From 200 to $\sim$ 300 km the PV exhibits a strong gradient close to 70° at the winter solstice, which precludes barotropic instability (and hence eddy-mixing) from occurring at high latitudes. The gradient is much weaker at lower latitudes and in the summer hemisphere. The time scales in Fig. 16b indicate that it is only close to summer that eddy mixing becomes effective. This is also consistent with the indication of a dark circumpolar collar at 70° in Voyager 2 images (Smith et al., 1981), which may indicate the edge of the vortex. The same pattern has been reported in the southern hemisphere, five years after spring equinox, from HST and ground-based images (Lorenz et al., 2001; Roe et al., 2002). At equinox the model tracer concentrations start to increase close to the south pole due to the subsiding MMC there, which brings tracers from
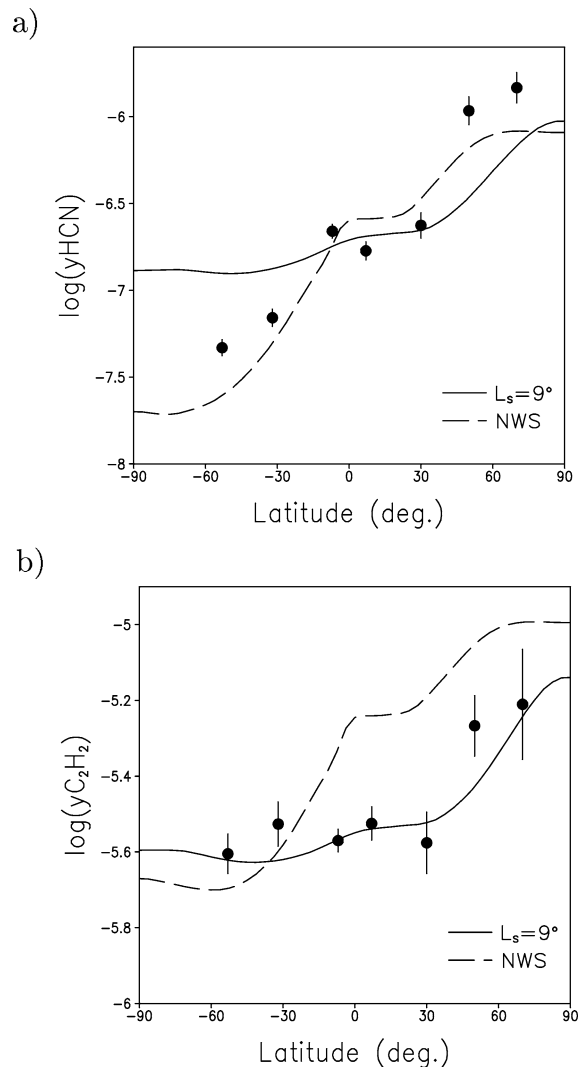
aloft. Although the distribution of $C_2H_2$ seems to agree with this, the discrepancy with the data for HCN suggests other factors, such as a seasonally-varying photochemistry, may play a role for this particular species.

## 5. Discussion

We have developed a numerical scheme to parameterize latitudinal eddy mixing by barotropic waves in Titan's atmosphere. The scheme has been implemented in a 2D, axially-symmetric GCM. The parameterization is adaptive, acting locally and in real time on both the flow and the passive tracers. Model results for wind speed, stratospheric temperatures and the latitudinal contrasts of trace species

agree well with observations. Eddy mixing is triggered by barotropic instability of the mean zonal flow, which in turn is created by the build-up of the winter jet in the subsiding branch of the Hadley cell. This occurs mainly on the equatorward flank of the jet and at midlatitudes in the summer hemisphere, at altitudes between 200 and 300 km. The model self-consistently reproduces the predictions of the 3D GCM (H95), with an augmented superrotation created by the coupling between the accumulation of haze at the poles due to the MMC, cooling and the resulting enhanced MMC. In the upper atmosphere, the same large-scale patterns are recovered in the present 2D model, including the wind inversion (from northward to southward) between $\sim 10$ and 30 mbar. Figures 8 and 9 can be compared with Figs. 6 and 8 of H95 (which extend only up to 0.3 mbar, or $\sim 240$ km in altitude). Lorenz et al. (2001) have reported on seasonal change of the North–South Asymmetry (NSA) of Titan's albedo. They note that at wavelengths originating deep in the atmosphere the NSA they observed in 2000 had not reversed relative to 1995 (southern spring equinox), but that at higher altitudes (above $\sim 60$ km) there was a clear reversal. Their results suggest an altitude-dependent phase lag of the seasonal cycle. Our wind inversion close to 30 mbar ($\sim 70$ km) is consistent with such a variation with altitude, but the phase lag of the albedo is a question that merits further investigation, since we observe no such lag in the circulation at deeper levels.

The prevailing models proposed to explain the hemispheric asymmetry of the stratospheric temperatures are based either on the dynamical inertia of the atmosphere (Flasar and Conrath, 1990), which would lead to mean meridional circulation lagging the solar forcing by a time of the order of the seasonal time scale, or on a non-uniform distribution of infrared opacity (Bézard et al., 1995). The model results privilege the latter hypothesis, since the response of the MMC is in phase with the radiative forcing at the unit optical depth level. The transport of the haze by the MMC into the polar region leads to a cooler winter pole at 1 mbar, and to an enhanced circulation (Rannou et al., 2003). For the same reason, the meridional wind speed in the upper stratosphere ($v \sim 0.1$ m s$^{-1}$) is higher than earlier estimates based on arguments of momentum and heat transfer which assumed a uniform haze opacity (Flasar et al., 1981; Flasar and Conrath, 1990). This implies a fast seasonal variation when the wind changes from northward to southward at equinox. The pole-to-pole travel time of the haze is of the order of $\pi a/v$, or $\sim 2.56$ terrestrial years, making the turnover time of the haze albedo about 5 years. This is consistent with the turnover recently observed in the high-altitude albedo (Lorenz et al., 2001; Roe et al., 2002).

The GCM provides important insight into the eddy-mixing time scale, and helps explain why latitudinal contrasts developed during winter tend to persist through spring. Rather than a purely photochemical effect such as the one pointed out by Yung (1987), our results suggest a dynamical origin of the contrasts. Firstly, the MMC enriches the

winter polar region with trace species coming from the high stratosphere, while the zonal winds simultaneously build the circumpolar vortex. On the other hand, whereas at solstitial epochs eddy mixing extends over large regions, with a time constant much less than a season, at equinoxes mixing is important only at the flank of the jet. Hence, during winter and spring the vortex isolates the pole from mixing occurring at lower latitudes, and it is only by late spring that mixing sets in and starts to erase the contrasts. This is consistent with a circumpolar collar at spring close to 70° (Smith et al., 1981; Lorenz et al., 2001; Roe et al., 2002) which may indicate the edge of the vortex. Relative to the previous model of Lebonnois et al. (2001), the more realistic coupling between the waves and the mean flow in the GCM leads to more homogeneous distributions of chemical species and haze at regions of barotropic instability, and to a better representation of the latitudinal contrasts of trace species. Therefore, our results suggest the observed contrasts at the winter high latitudes can be interpreted as a signature of non-axisymmetric motions, which are closely linked to the axisymmetric dynamics. The model also predicts an important variation of eddy mixing with altitude, with stronger mixing occurring only above 3 mbar during summer. Cassini should be able to observe both effects after its arrival to the Saturn system in July 2004.

We have presented results from the first GCM of Titan's atmosphere coupling atmospheric dynamics, haze microphysics, a simplified photochemistry and the effects of non-axisymmetric eddies. Given the paucity of the available data, our results alone do not constitute a proper validation of the model for future experiments. However, the agreement with observations (also analyzed in the companion papers by Rannou et al., 2002, 2003, and Lebonnois et al., 2003) is encouraging. At its present state the model reconciles observations of stratospheric temperature, wind speed and chemical composition and gives a unified view of the interplay between different processes. The expected retrieval of more data by Cassini-Huygens in the years to come will allow to constrain the model parameters and improve predictions even more.

# References

Allison, M., Del Genio, A.D., Zhou, W., 1994. Zero potential vorticity envelopes for the zonal-mean velocity of the Venus/Titan atmospheres. J. Atmos. Sci. 51 (5), 694–702.

Andrews, D.G., Holton, J.R., Leovy, C.B., 1987. Middle Atmosphere Dynamics. Academic Press, San Diego, CA.

Bézard, B., Coustenis, A., McKay, C.P., 1995. Titan's stratospheric temperature asymmetry: a radiative origin. Icarus 113, 267–276.

Botet, R., Rannou, P., Cabane, M., 1997. Mean-field approximation of Mie scattering by fractal aggregates. Appl. Optics 36, 8791–8797.

Cabane, M., Chassefière, E., Israel, G., 1992. Formation and growth of photochemical aerosols in Titan's atmosphere. Icarus 96, 176–189.

Charney, J.G., Stern, M., 1962. On the stability of internal baroclinic jets is a rotating atmosphere. J. Atmos. Sci. 19, 159–172.

Coustenis, A., Bézard, B., 1995. Titan's atmosphere from Voyager infrared observations. IV. Latitudinal variations of temperature and composition. Icarus 115, 126–140.

Del Genio, A.D., Zhou, W., 1996. Simulations of superrotation on slowly rotating planets: sensitivity to rotation and initial condition. Icarus 120, 332–343.

Del Genio, A.D., Zhou, W., Eichler, T.P., 1993. Equatorial superrotation in a slowly rotating GCM—implications for Titan and Venus. Icarus 101, 1–17.

Flasar, F.M., 1998a. The composition of Titan's atmosphere: a meteorological perspective. Planet. Space Sci. 46, 1109–1124.

Flasar, F.M., 1998b. The dynamic meteorology of Titan. Planet. Space Sci. 46, 1125–1147.

Flasar, F.M., Conrath, B.J., 1990. Titan's stratospheric temperatures: a case for dynamical inertia. Icarus 85, 346–354.

Flasar, F.M., Conrath, B.J., 1992. The meteorology of Titan. In: Symposium on Titan. In: ESA SP, Vol. 338. ESA, European Space Agency, pp. 89–99.

Flasar, F.M., Samuelson, R.E., Conrath, B.J., 1981. Titan's atmosphere: temperature and dynamics. Nature 292, 693–698.

Gierasch, P.J., 1975. Meridional circulation and the maintenance of the Venus atmospheric rotation. J. Atmos. Sci. 32, 1038–1044.

Hitchman, M.H., Leovy, C.B., Gille, J.C., Bailey, P.L., 1987. Quasi-stationary zonally-asymmetric circulations in the equatorial lower mesosphere. J. Atmos. Sci. 44, 2219–2236.

Hourdin, F., Armengaud, A., 1998. On the use of finite volume methods for atmospheric advection of trace species. I. Test of various formulations in a General Circulation Model. Mon. Weather Rev. 127 (5), 822–837.

Hourdin, F., Le Van, P., Talagrand, O., Courtin, R., Gautier, D., McKay, C.P., 1992. Numerical simulation of the circulation of the atmosphere of Titan. In: Symposium on Titan. In: ESA SP, Vol. 338. ESA, European Space Agency, pp. 101–106.

Hourdin, F., Talagrand, O., Sadourny, R., Courtin, R., Gautier, D., McKay, C.P., 1995. Numerical simulation of the general circulation of the atmosphere of Titan. Icarus 117, 358–374.

Hubbard, W.B., 45 colleagues, 1993. The occultation of 28 Sgr by Titan. Astron. Astrophys. 269, 541–563.

Hunt, B.G., 1981. The maintenance of the zonal mean state of the upper atmosphere as represented in a three-dimensional general circulation model extending to 100 km. J. Atmos. Sci. 38, 2172–2186.

Kostiuk, T., Fast, K.E., Livengood, T.A., Hewagama, T., Goldstein, J.J., Espenak, F., Buhl, D., 2001. Direct measurement of winds on Titan. Geophys. Res. Lett. 28, 2361–2364.

Lebonnois, S., Toublanc, D., Hourdin, F., Rannou, P., 2001. Seasonal variations of Titan's atmospheric composition. Icarus 152, 384–406.

Lebonnois, S., Hourdin, F., Rannou, P., Luz, D., Toublanc, D., 2003. Impact of the seasonal variations of composition on the temperature field of Titan's stratosphere. Icarus 163, 164–174.

Lellouch, E., Hunten, D.M., Kockarts, G., Coustenis, A., 1983. Titan's atmosphere profile. Icarus 83, 308–324.

Lellouch, E., Coustenis, A., Gautier, D., Raulin, F., Dubouloz, N., Frère, C., 1989. Titan's atmosphere and hypothesised ocean: a reanalysis of the Voyager 1 radio-occultation and IRIS 7.7 µm data. Icarus 79, 328–349.

Lorenz, R.D., Young, E.F., Lemmon, M.T., 2001. Titan's smile and collar: Hst observations of seasonal change 1994–2000. Geophys. Res. Lett. 28 (23), 4453–4456.

Luz, D., Hourdin, F., 2003. Latitudinal transport by barotropic waves in Titan's stratosphere. I. General properties from a horizontal shallow-water model. Icarus 166, 328–342.

McKay, C.P., Pollack, J.B., Courtin, R., 1989. The thermal structure of Titan's atmosphere. Icarus 80, 23–53.

Rannou, P., Cabane, M., Chassefière, E., Botet, R., 1997. A new interpretation of scattered light measurements at Titan's limb. J. Geophys. Res. 102, 10997–11013.

Rannou, P., Hourdin, F., McKay, C.P., 2002. A wind origin for Titan's haze structure. Nature 418, 853–856.

Rannou, P., Hourdin, F., McKay, C.P., Luz, D., 2003. A coupled dynamics-microphysics general circulation model of Titan's atmosphere. Icarus. Submitted for publication.

Roe, H.G., de Pater, I., Macintosh, B.A., Gibbard, S.G., Max, C.E., McKay, C.P., 2002. Note: Titan's atmosphere in late southern spring observed with adaptive optics on the W.M. Keck II 10-meter telescope. Icarus 157, 254–258.

Rossow, W.B., Williams, G.P., 1979. Large-scale motion in the Venus stratosphere. J. Atmos. Sci. 36 (3), 377–389.

Sadourny, R., 1975. Compressible model flows on the sphere. J. Atmos. Sci. 32, 2103–2110.

Schoeberl, M.R., Hartmann, D.L., 1991. The dynamics of the stratospheric polar vortex and its relation to springtime ozone depletions. Science 251, 46–52.

Smith, B.A., Soderblom, L., Beebe, R.F., Boyce, J.M., Briggs, G., Bunker, A., Collins, S.A., Hansen, C., Johnson, T.V., Mitchell, J.L., Terrile, R.J., Carr, M.H., Cook, A.F., Cuzzi, J.N., Pollack, J.B., Danielson, G.E., Ingersoll, A.P., Davies, M.E., Hunt, G.E., Masursky, H., Shoemaker, E.M., Morrison, D., Owen, T., Sagan, C., Veverka, J., Strom, R., Suomi, V.E., 1981. Encounter with Saturn—Voyager 1 imaging science results. Science 212, 163–191.

Sromovsky, L.A., Suomi, V.E., Pollack, J.B., Krauss, R.J., Limaye, S.S., Owen, T., Revercomb, H.E., Sagan, C., 1981. Implications of Titan's north–south brightness asymmetry. Nature 292, 698–702.

Toon, O.B., McKay, C.P., Ackerman, T.P., Santhanam, K., 1989. Rapid calculation of radiative heating rates and photodissociation rates in inhomogeneous multiple scattering atmospheres. J. Geophys. Res. 94, 16287–16301.

Toublanc, D., Parisot, J.P., Brillet, J., Gautier, D., Raulin, F., McKay, C.P., 1995. Photochemical modeling of Titan's atmosphere. Icarus 113, 2–26.

van Leer, B., 1977. Towards the ultimate conservative difference scheme. V. A second-order sequel to Godunov's method. J. Comput. Phys. 23, 276–299.

Yelle, R.V., 1991. Non-LTE models of Titan's upper atmosphere. Astrophys. J. 383, 380–400.

Yung, Y.L., 1987. An update of nitrile photochemistry on Titan. Icarus 72, 468–472.